A Customizable Thermographic Imaging System for Medical Image Acquisition and Processing

Juan A. Leñero-Bardallo, *Member, IEEE*, Rafael de la Rosa-Vidal, Rubén Padial-Allué, Joaquín Ceballos-Cáceres, Ángel Rodríguez-Vázquez, *Fellow, IEEE*, and José Bernabéu-Wittel

***Abstract*— A custom system has been developed for medical image acquisition and processing in both the visible and the infrared (IR) bands. Unlike some non-customizable commercial devices, this system can easily be adapted to different application scenarios by adding new peripherals and/or custom image processing algorithms. Portable, autonomous, and easy to use, it offers immediate results at the moment of examination and has a competitive cost. The system comprises a Single Board Computer (SBC) controlling a group of sensors and peripherals. The hardware implementation, described in detail in this paper, was adapted for two different application scenarios. First, the system was employed to differentiate between different kinds of vascular anomalies. The clinical results obtained are reported. The device was then redesigned to automatically detect people with high body temperatures in public environments. The system's real-time image processing capabilities in both scenarios are demonstrated. Specific algorithms were implemented by the authors for each case study.**

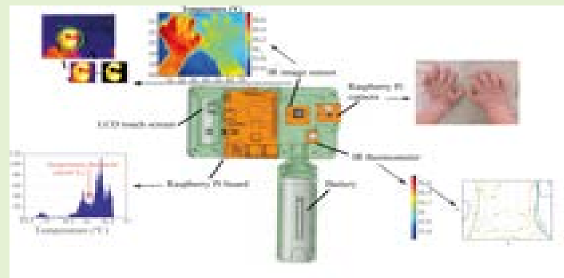

***Index Terms*— Body temperature detection, Image Processing, LWIR, Medical sensors, Raspberry Pi board, Thermographic imaging, Vascular anomaly.**

I. Introduction

OVER the last ten years, infrared cameras have become more affordable. The current COVID-19 pandemic has significantly increased demand for them and as a result they are now being deployed on a massive scale in public places like airports, stadiums, and train stations to detect individuals with fever. Clinically, they can also be used to obtain very accurate body temperature measurements. Prior to the pandemic, several authors had already drawn attention to their great potential for biomedical applications in many fields where accurate body temperature analysis is decisive [1]–[3]. Infrared cameras are generally acknowledged as an excellent solution for studying local body temperature variations in different clinical conditions such as hemangiomas [1], [4], [5], burns [1], extremity thrombosis [1], and other temperature related conditions [1], [2]. Indeed, providers like Meditherm [6] and Spectron IR [7] are already offering infrared cameras specifically targeted towards the medical field.

One unexplored field that could benefit from these emerging devices is the correct classification of vascular anomalies [8]. Some of these anomalies alter local hemodynamics and temperatures. Classification of vascular anomalies by visual inspection is challenging even for experts. Traditionally, it relies on examinations using Doppler ultrasonography or magnetic resonance imaging (MRI) [9], neither of which take into account temperature variations. However, these forms of medical imaging require trained operators and are not always immediately available for clinical use.

In clinical scenarios, imaging systems must satisfy several requirements: they must be accurate, portable, easy to use, and autonomous, and their results must be easy to interpret. Images in the visible spectrum can provide extra information about texture and color that is of key importance in medical specialties like dermatology. They are also helpful for identifying patients and injured body regions. Multispectral imaging in both the visible and infrared (IR) bands is therefore a must. Finally, the incorporation of extra peripherals and sensors into an imaging system facilitates its adaptability to different medical scenarios.

In this article, we present an open, customizable, general-purpose platform for measuring body temperature. This platform was designed to be adaptable to different scenarios

This study was supported by programmes and projects: Ayudas a Proyectos de I+D+I Programa Operativo FEDER through Project US-1264940; Proyecto Singular de Transferencia del Conocimiento: Ecosistema Innovador con Inteligencia Artifial para Andalucía 2025 CEI-07; Spanish Government MINECO and European Regional Development Fund, (ERDF/FEDER) through Project RTI2018-097088-B-C31; ONR grant ONR NICOP N00014-19-1-2156; and by EU H2020 MSCA ACHIEVE-ITN, Grant No 765866.

Juan A. Leñero-Bardallo, Rafael de la Rosa-Vidal, Á. Rodríguez-Vázquez, and J. Ceballos-Cáceres are with the Institute of Microelectronics of Seville (IMSE-CNM), CSIC-Universidad de Sevilla, Spain (E-mails: {jlenero,rdvidal,arodri-vazquez}@us.es and joaquin@imse-cnm.csic.es.)

Rubén Padial-Allué works at MAHLE Electronics, Valencia, Spain, (E-mail: padialruben@gmail.com.)

José Bernabéu-Wittel works at the Dermatology Unit of the hospital Virgen del Rocío, Spain, (E-mail: jbernabeuw@gmail.com).

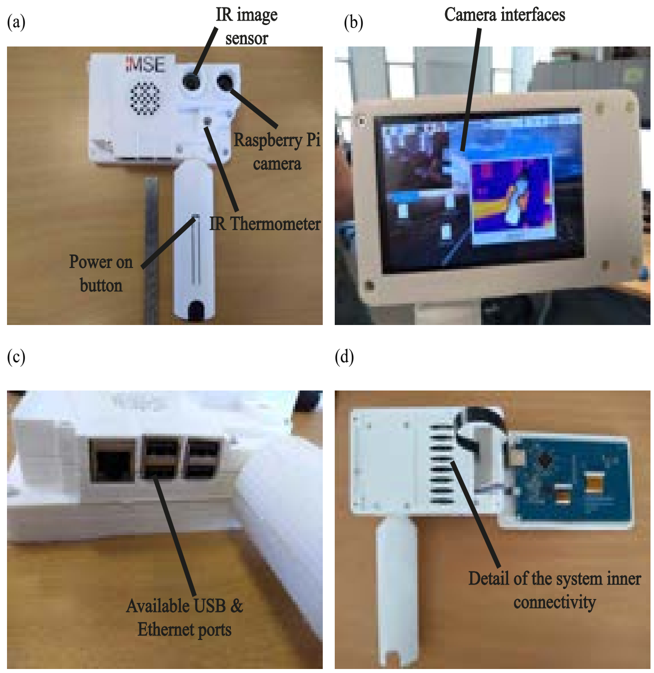

Fig. 1. Detail of the system's final implementation. (a) Front view. Main system components have been highlighted. (b) Back view displaying the two image sensor interfaces operating in parallel. (c) Lateral view showing the available Ethernet and USB ports. (d) Detail of the internal connectivity with the touch screen.

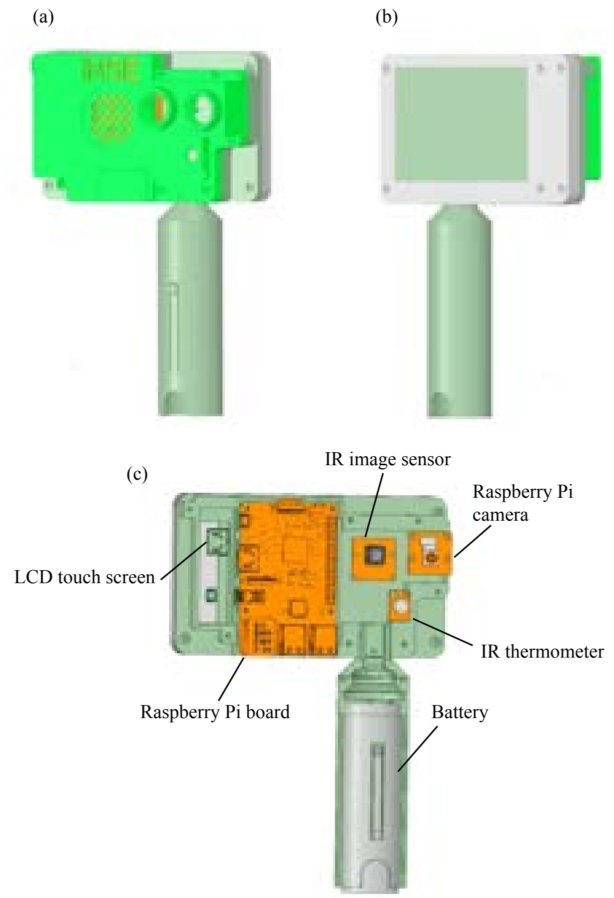

Fig. 2. The system's casing design. (a) Rear view. (b) Front view. (c) Main components assembly. The battery can be easily replaced by pulling it up/down through the stick.

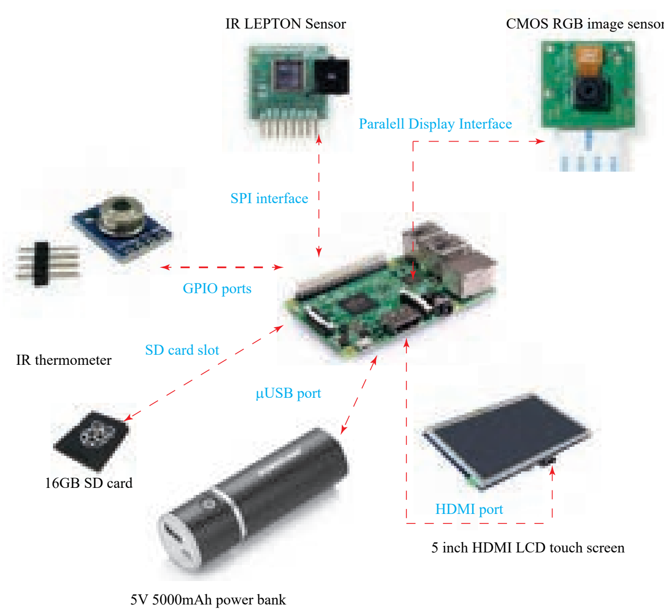

Fig. 3. Illustration of the system's components. The Raspberry Pi 3 board is in the centre, and the different sensors and peripherals are connected to it.

in which IR images can provide thermal information. The system can be expanded by adding additional sensors and peripherals, it can display real-time images, and it can run image processing algorithms. To demonstrate its applicability, we used it to classify vascular malformations in both high- and low-flow cases and to automatically detect people with high body temperatures in public places.

II. System implementation

A. Overview and mechanical design

The generic system implementation can be seen in Figure 1.(a)-(d), which shows the position of its peripherals and sensors. To house and protect the system components, a casing was designed and fabricated with a 3D printer fed with PLA filament. Figure 2 details the casing design, providing front and rear view. There were several design requirements: 1) The system had to be easy to handle during clinical sessions. 2) The battery had to be easily replaceable. 3) Low weight. 4) The system's USB and Ethernet ports had to be accessible to connect the system with other devices such as external memories or computers. 5) The system had to allow power dissipation and cooling. Figures 2(a) and 2(b) show front and rear views of the casing, respectively. Figure 2(c), details the internal layout, showing how the main components were assembled.

B. System components

Figure 3 shows all the system's components. For the sake of simplicity, we will describe the function of each one separately:

- Raspberry Pi 3 B+ board. This is the main element of the system. It controls all the peripherals and processes and stores, and transmits visual information. It can also run dedicated image processing algorithms to process captured images. It runs the Linux-based operating system Raspbian and some dedicated scripts programmed in C++ and Python languages. All the sensors and the battery are connected to the Raspberry Pi board as shown in Figures 4 and 5. The board has a 40-pin GPIO connector, USB ports, a CSI-2 camera interface, WiFi, and Bluetooth connectivity.
- Lepton IR image sensor. This is the most important sensor in the system. It is connected to the Raspberry Pi board via a 40-pin connector. After calibration, it provides absolute temperature values for the visual scene. A dedicated interface is capable of recording and displaying real-time images in the LWIR (Long Wave Infrared) band. The sensor is intended to classify the vascular anomalies under study and/or to determine their size.
- Raspberry Pi image sensor. This sensor captures visible band images of all the patients under study. Although the information in this band was not important in this study, it is useful to keep a record of the patient's anomaly and be able to compare its features in the visible and LWIR bands simultaneously. Images in the visible band provide complementary information about things like texture and color. A dedicated interface records and displays real-time visible band images and videos.
- Melexis MLX90614D IR thermometer. This has the job of calibrating the IR sensor to translate radiation levels into thermographic images. It takes absolute temperature measurements without touching patients.
- 5-inch HDMI LCD screen. To simultaneously display real-time images in the visible or LWIR bands.
- External battery. The entire system can operate autonomously for more than 5.5 hours.
- External SD memory.

C. System connectivity

Figures 4 and 5 show the Raspberry Pi's connectivity with all the system peripherals. Figure 4.(a) details the ports and interfaces that each device uses to send/receive data. In Figure 4.(b), there is a diagram showing the data flow between the developed sensors and software interfaces. Figure 5 shows the connections made via the Raspberry Pi's 40-pin GPIO port.

The IR image sensor uses the Raspberry Pi SPI interface for video streaming and the I^2C interface for communication with the sensor interface installed on the Raspberry Pi board. The Raspberry Pi image sensor is connected via the Camera Serial Interface (CSI-2), the dedicated image sensor connection interface. The touch screen is connected via the available HDMI connector for video streaming, with one USB port being used for the touch screen driver embedded in the device. The IR thermometer is connected to the Raspberry Pi connector. It uses one power supply pin, and two general-purpose I/O ports to transmit or receive data using the I^2C protocol. Any of the

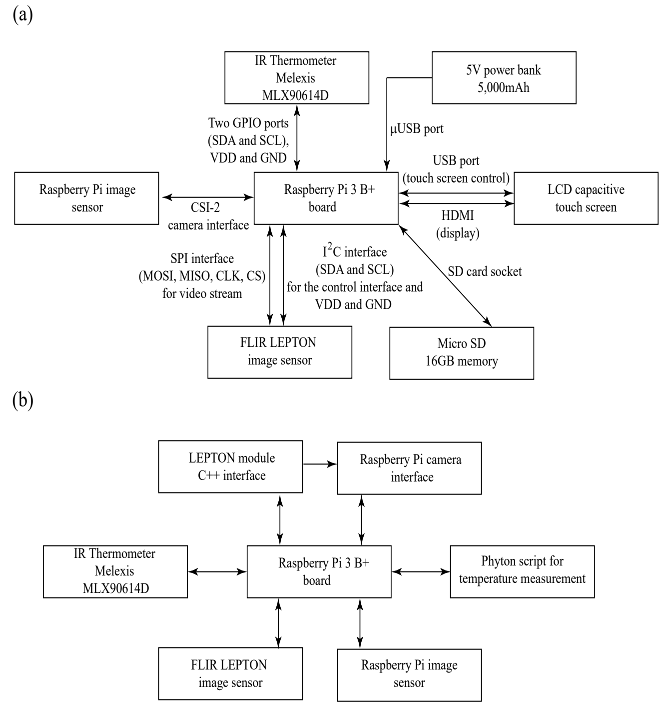

Fig. 4. (a) Detailed hardware system connectivity. (b) Scheme of the interfacing data flow between the three sensors that compound the system.

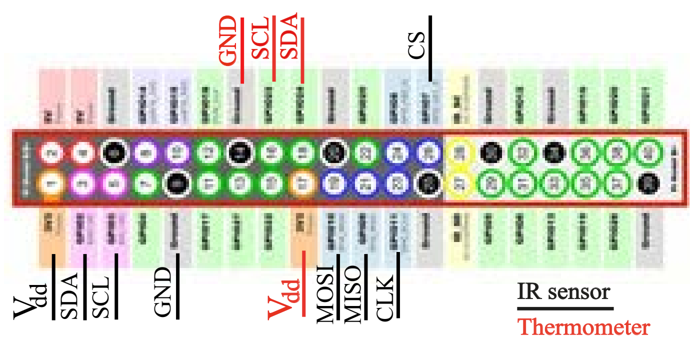

Fig. 5. Details of the Raspberry Pi's 40-pin bus connectivity. Connections with the IR image sensor are plotted in black. Connections with the IR thermometer are marked in red.

Raspberry Pi's free USB ports and wireless interfaces can be employed to download data stored during the clinical sessions or to add external memories or peripherals. The battery is connected directly to the power supply µUSB port.

D. System specifications

The most important system specifications are summarized in Table I. Thanks to the Broadcom BCM2837B0 CPU and the 64-bit dedicated GPU, the system has high image processing capabilities. The SD memory has sufficient capacity to store images and video over multiple clinical sessions. The system's possibilities for connecting with other devices and peripherals are numerous, with three available USB ports, WiFi

TABLE I
SYSTEM SPECIFICATIONS

CPU	Broadcom BCM2837B0
GPU	Cortex-A53 64-bit SoC@1.4GHz
RAM	1GB LPDDR2 SDRAM
Power consumption	890mA@5V
Autonomy	>5.5 hours
IR sensor resolution	160×120 pixels
IR sensor frame rate	at least 2fps
RGB sensor frame rate	1920×1080@30fps
RGB sensor resolution	3280×2464 pixels (static images)
Weight	550 grams (including battery)
Temperature accuracy	0.1°C after calibration
Screen resolution	800×480
WiFi connectivity	yes
Bluetooth connectivity	yes
Ethernet connectivity	yes
Operating system	Raspbian

TABLE II
COST OF SYSTEM COMPONENTS

Raspberry Pi 3 B+ board	35€
16GB SD memory card	15€
5 INCH HDMI LCD touch screen	42€
Power bank 5,000mAh	10€
MELEXIS infrared thermometer	5€
LEPTON infrared sensor	245€
Raspberry Pi camera	30€
HDMI connectors and buses	10€
3D printer material	5€
TOTAL	397€

and Bluetooth wireless connectivity, and an Ethernet port. Table II summarises of the approximate cost of the system's components. The total cost of the components and material is below 400€.

III. IR SENSOR CALIBRATION

To render IR images, infrared radiation levels measured by the IR sensor have to be translated into absolute temperature values. The Melexis MLX90614D IR thermometer was mounted in the system for precisely this purpose. Optimized to operate within a temperature range of $[22, 40]$ °C, and compatible with medical body temperature measurements, the device is factory calibrated. It simultaneously measures both skin and ambient temperatures. The skin temperature measurement is corrected taking into account the ambient temperature. For this purpose, the vendor has integrated a DSP device in the sensor. The calibration procedure consists of taking two temperature measurements at two different body locations, e.g., the palm and the forehead. A C routine was implemented to automatize the calibration procedure. Two snapshots were taken and their temperatures measured. According to the vendor, the dependence between radiation levels and absolute temperatures is linear in the operating range. Knowing the temperature of two different body spots, T_1 and T_2 and their respective radiation levels R_1 and R_2, it was therefore possible to determine the linear relationship between the radiation levels and the absolute temperatures, as depicted in in Listing I.

Listing I: Infrared image sensor calibration procedure.

1) We measured the absolute temperature T at a fixed distance from two different body spots with uniform temperature (for instance, the forehead and the palm). The temperatures of each spot were denoted T_1 and T_2.
2) We used the IR image sensor to measure the average infrared (IR) levels in the LWIR band at the same spots and at the same distance. The radiation levels of each spot were denoted IR_1 and IR_2.
3) To determine the a and b constants, the following equation system was solved:

$$\begin{aligned} T_1 &= a \cdot IR_1 + b, \\ T_2 &= a \cdot IR_2 + b \end{aligned} \quad (1)$$

4) The sensor radiation levels were translated into temperature levels using the following equation:

$$T = a \cdot IR + b \quad (2)$$

The calibration procedure described in Listing I provides accurate temperature measurements if the readings are taken at a fixed distance from the IR camera. The infrared radiation flux emitted by an object decreases quadratically with distance. In practical situations, the target will not be at a fixed distance. In Figure 6, absolute temperature error was plotted against distance. In this experiment, absolute temperature was measured with the Melexis MLX90614D thermometer at an initial distance of 40 cm from the target (a person's bare forehead). Absolute error is represented in the blue trace, while the red trace contains the best non-linear data fitting, in accordance with the following law:

$$\epsilon(d) = \alpha - \beta \frac{1}{d^{\gamma}} \quad (3)$$
$$with \;\; \alpha = -1.89 \;\; \beta = 12.06 \;\; \gamma = 0.4393$$

The maximum distance at which the device can gauge temperature depends on three factors: the device's optics, the device's IR pixel resolution, and the size of the object to be measured. Following the manufacturer's indications, we took measurements within a region of interest larger than 3×3 pixels. Error dependence with distance is also conditioned by other factors: the quadratic decay of IR radiation with distance, the size of the object, the pixels' sensing of different radiation levels depending on distance, and the effect of the object's curvature on the optical projection of the visual scene on the sensor's pixels. It is therefore challenging to take absolute temperature measurements if the distance to the target is unknown. Fortunately, operating within a certain range of the lens, the measured error is acceptable in many application scenarios.

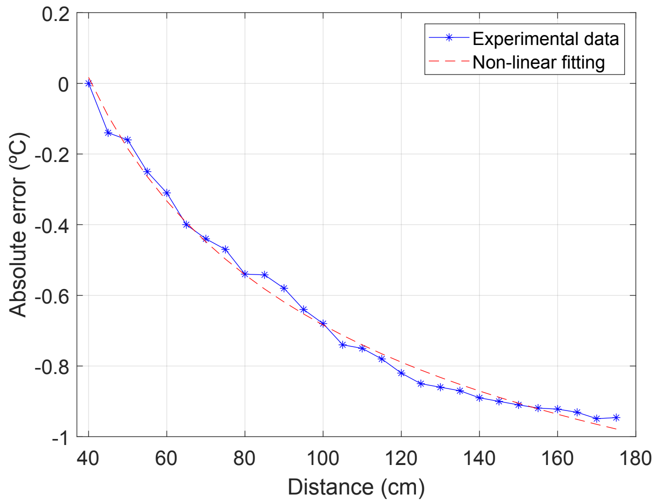

Fig. 6. Absolute temperature error versus distance between the target and the device. Blue trace: experimental results. Red trace: best non-linear data fitting.

IV. Case study A: A differentiation of vascular anomalies

Vascular anomalies constitute a very wide spectrum of disorders [10], [11]. For some of them, correct classification is a real challenge. In many cases, they have to be analyzed by different specialists to obtain the correct early diagnosis which will be crucial for their treatment. A simple classification of vascular anomalies establishes two main families: vascular malformations and vascular tumors. The former include low-flow and high-flow malformations, while the latter include hemangiomas, a vascular anomaly very common among infants [12]. The proposed case study focused on differentiating between low-flow and high-flow malformations, and on estimating the area of high-flow malformations and hemangiomas. Over sixty vascular malformations and over 100 hemangiomas were studied for two years. The research was approved by the Hospital Virgen del Rocío Review Board. Beforehand, the participants' representatives also signed a consent form allowing the study to be carried out.

A. High- and low-flow vascular malformation analysis

High- and low-flow vascular malformations [10], [11] may appear very similar when examined visually [8]. [8]. Their prognosis, however, is completely different. High-flow malformations are potentially more dangerous. Moreover, their hemodynamic flow is different. They are created by arteriovenous malformations, and the blood flow inside them is therefore high. This increases the temperature locally. Low-flow malformations are caused by venous and capillary malformations. The blood flow inside them —and therefore their temperature— is lower.

This study differentiated vascular malformations by analyzing their temperature, an approach completely different to that of traditional methods, which are mainly based on Doppler ultrasonography or magnetic resonance [9]. Figure 7 shows a case study of two different vascular malformations at similar places on the left hands of two different patients. Figures 7(a),(c) are images in the visible spectrum. The arrows indicate the exact location of the affected region in each case. Both malformations are very similar and are impossible to differentiate by visual inspection. Figures 7(b),(d) are thermographic images in the LWIR band. Here, the temperature patterns of the two malformations are completely different. For the high-flow malformation shown in Figures 7(a),(b), the temperature of the injured region is higher. Moreover, the malformation reduces the blood flow in the other limb, so there is clear asymmetry between the temperatures of the two hands (up to 0.7 °C in some places). Similar temperature asymmetry can be observed between the injured and non-injured fingers.

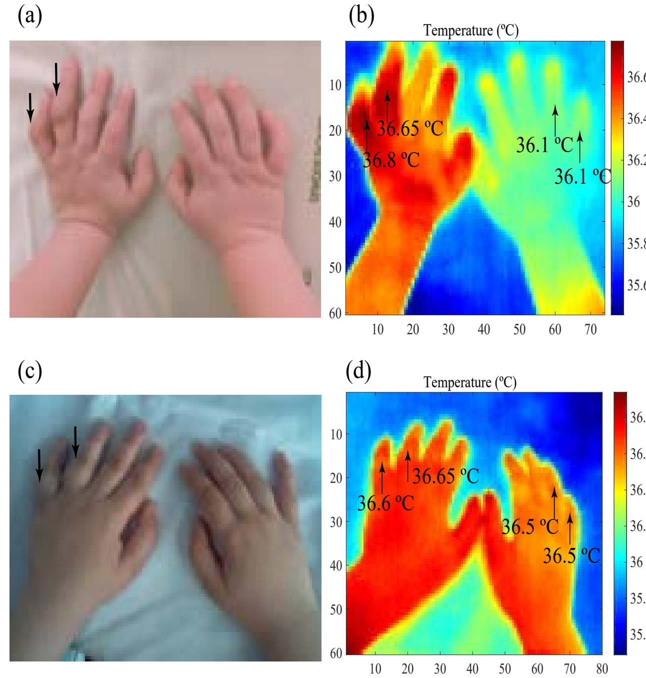

Fig. 7. Comparative analysis of high- and low-flow vascular malformations in the hand. Arrows indicate the malformation locations. (a)-(c) are images in the visible spectrum. (b)-(d) are thermal images acquired with the IR image sensor. (a)-(b) correspond to high-flow malformations. (c)-(d) correspond to low-flow malformations.

We analyzed more than 60 vascular malformations of different types. All of them had been diagnosed and classified previously. In all cases, it was possible to correctly classify the malformations by establishing a temperature threshold. High-flow malformations create temperature variations in the [0.45 °C, 0.8 °C] range, low-flow malformations in the [-0.3 °C, 0.25 °C] range. The 99% confidence intervals do not overlap, so a temperature decision boundary can be set to classify the two types.

B. Study and prognosis of hemangiomas

Infantile hemangiomas are benign tumors produced by the proliferation of endothelial cells of blood vessels. Incidence is high (4%-10%) in children under the age of one year [12], [13]. These tumors are not included in the vascular malformations studied previously. The capillary and venous

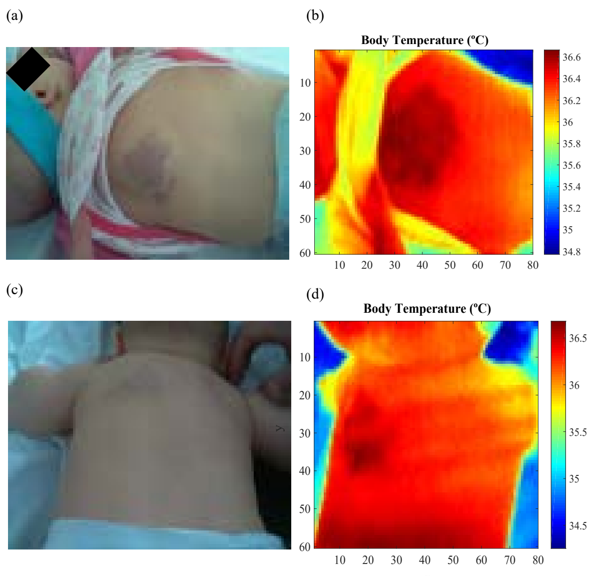

Fig. 8. Hemangioma before (images (a) and (b)) and after (images (c) and (d)) treatment. The thermographic image helps to determine whether the tumor has decreased after treatment and, accordingly, to select the correct dose of propranolol.

effects associated with them cause variations in temperature [1]. Early detection and treatment of hemangiomas are crucial to reduce their impact. Nowadays, they are successfully treated with oral propranolol [12]. Hemangiomas are diagnosed and subsequently assessed by visual inspection. No automated procedures exist for assessing their prognosis. In this case, the implemented system proved to be useful in monitoring their evolution and size after treatment.

Figure 8 shows an example of a hemangioma before and after treatment. Since not all the regions affected by the hemangioma are close to the skin and thus perceivable by visual inspection, the thermographic image is more capable of determining the size of the affected region. The dose of propranolol administered depends on the size of region affected by the hemangioma and on the patient's response to prior treatment [12]. To determine the optimum dose, it is therefore necessary to quantify the size of the injured region.

C. Comparison with classic forms of medical imaging

Figure 9 compares different types of medical images for two high-flow malformations located on the hand and the back, respectively. The left-hand column has images taken in the visible spectrum. The next column has infrared thermographic images, and the third has Doppler ultrasonography echographs. The fourth column has magnetic resonance images. Both the infrared images and the Doppler images provide equivalent results, indicating the regions with higher hemodynamic flow based on different physical properties. Ultrasonography measures the velocity of the blood flow, detecting whether vessels flow toward (blue) or away from (red) the transducer. Infrared imaging detects local temperature variations caused by changes in blood flow pressure. Magnetic resonance imaging is helpful in analyzing the extension and the depth of the malformation. From this analysis, it can be said that all the image types are complementary and non-exclusive. Infrared imaging has the advantage of being easy to interpret, and can be used during a first clinical examination for a fast diagnosis. Doppler ultrasonography and magnetic resonance require advanced equipment and trained operators that are not always available at the patient's first examination, thus limiting an early diagnosis. These last two techniques also inevitably involve touching the patient and the use of gels, and infants may therefore be apprehensive towards them.

D. Medical image processing

The SBC allows the implementation of real-time image processing algorithms. Several algorithms were implemented in the $C++$ language to process the thermal images. The capability of pre-programmed custom image processing algorithms to extract additional information from recorded images is one of the system's key advantages.

Contrast detection: The extraction of spatial contrasts from thermographic images after calibration provides information about the temperature gradients of adjacent body regions with different temperatures [14], [15]. Figure 10 shows an example obtained after processing one of the medical images shown previously in Figure8. In the left-hand column, we see an image of a vascular malformation in the visible spectrum. The middle column has a thermographic image after calibration, while the right-hand column shows a spatial contrast image. The values represent the temperature gradient of each pixel with respect to its neighborhood. These plots provide very accurate information about temperature gradients that is helpful in monitoring the patient's condition and in identifying the regions with higher vascular activity within the malformation. To extract the thermal gradients in the image, we used a Sobel-Feldman operator kernel [14], [15] applied after rendering one frame. The kernel's values were:

$$K = \begin{pmatrix} 47 & 0 & -47 \\ 162 & 0 & -162 \\ 47 & 0 & -47 \end{pmatrix} \tag{4}$$

Image segmentation: In some situations, it is desirable to isolate and/or highlight the region affected by the anomaly for further image processing. For this purpose, thresholding algorithms based on analysis of the image histogram prove useful. One such method, Otsu's algorithm [14], [15], determines the optimum temperature threshold to be applied to an image with an approximate bimodal distribution. The aim is to separate the patient's skin from regions with lower temperatures, i.e., the scene background, clothes, adornments, etc.

Figure 11 details the effect of Otsu's method before and after its application to a thermal image. The original image, shown in Figure 11(a), contains temperature data for regions that are irrelevant for medical study: i.e., the background and the parts of the body covered by garments. Figure 11(b) shows the image histogram. It can be seen that the histogram has two clearly distinguishable modes, corresponding to the

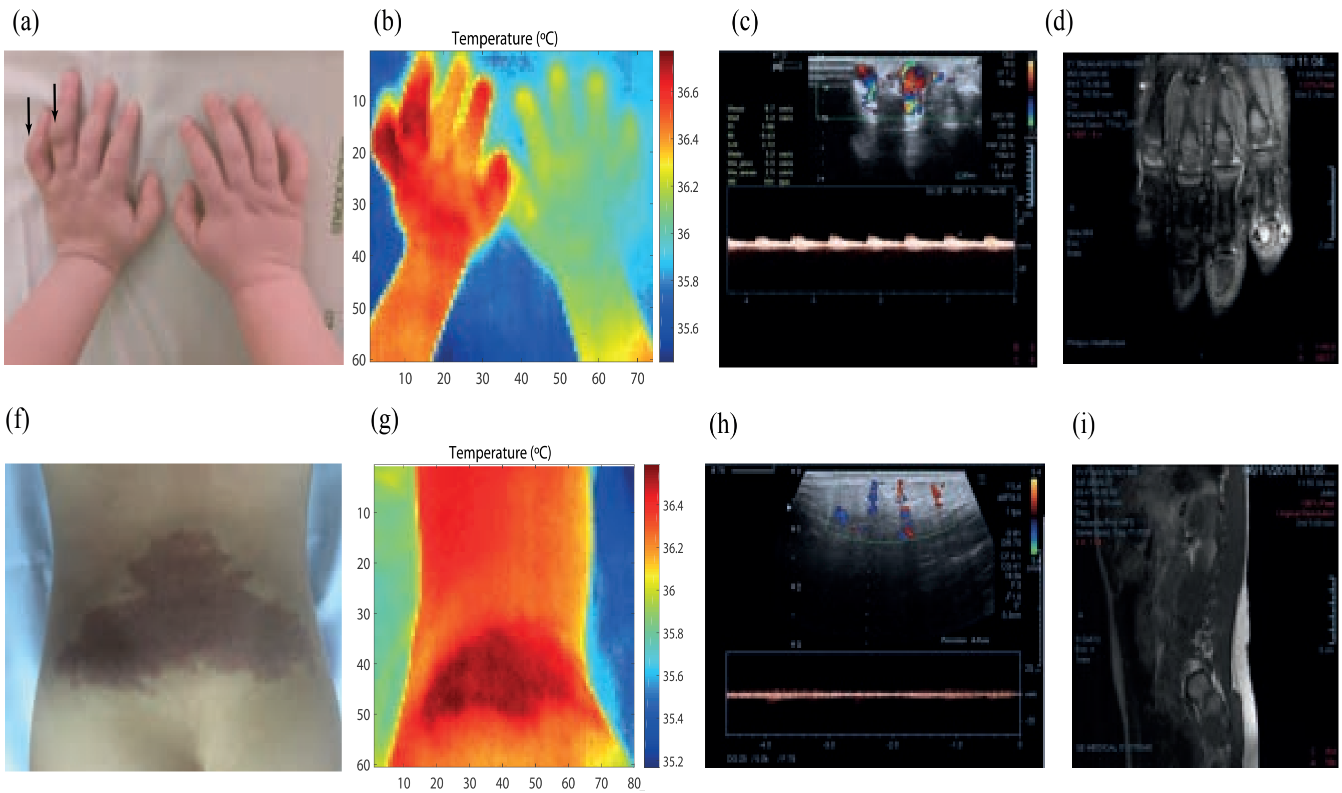

Fig. 9. Comparison between different types of medical imaging for high-flow vascular malformations. From left to right: images in the visible spectrum, thermographic images, Doppler ultrasonography images, and magnetic resonance images.

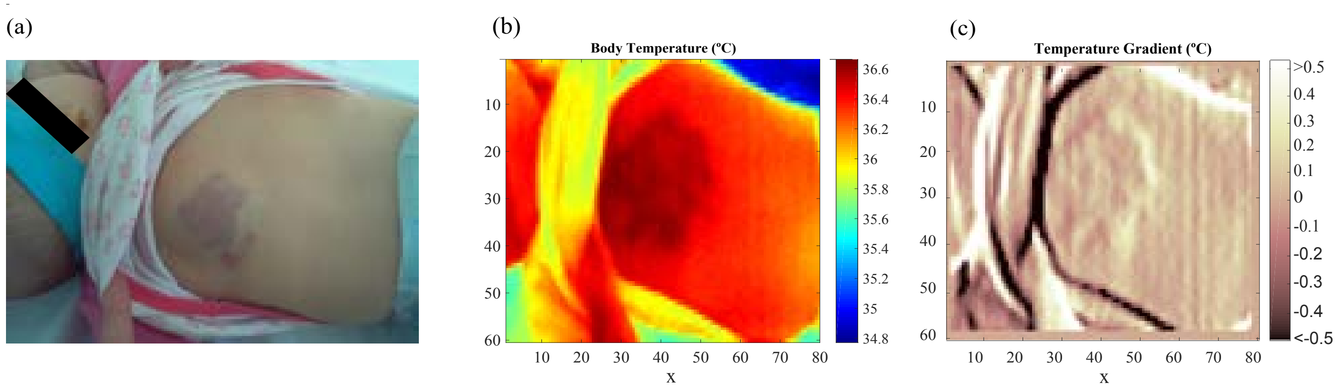

Fig. 10. Example of a contrast-detection algorithm applied to thermographic images. The resulting image provides information about the temperature gradient of each pixel with respect to the adjacent ones. The left-hand column has an image of the malformation in the visible spectrum. The middle column has a thermographic image of the malformation. The right-hand column has the image obtained after spatial contrast detection.

skin and to the scene's background temperatures. The optimum threshold value found by the algorithm is indicated by an arrow. The algorithm seeks the value that maximizes the deviation between the background and body histograms superposed on it. Figure 11(c) shows the segmented image after thresholding. The regions that are meaningless for the study—i.e., the background and the parts of the body covered by clothes—are shown in dark blue. As can be seen, the regions lacking in interest for our study have been correctly removed. The step-by-step procedure for segmenting the image is described in Listing II.

1) Temperature contour lines and area evaluation of vascular anomalies:: To track a patient's response to treatment, it may be more convenient to process off-line snapshots of images taken previously. Contours are curves joining all the continuous points (along a boundary) that have the same temperature or intensity. They are a useful tool for shape analysis and object detection and recognition. To obtain the temperature contour lines, we used predefined OpenCV [16] functions for contour extraction in conjunction with some basic image processing operations. Figure 12 shows how the contour lines were used to track the evolution of a hemangioma. Figures

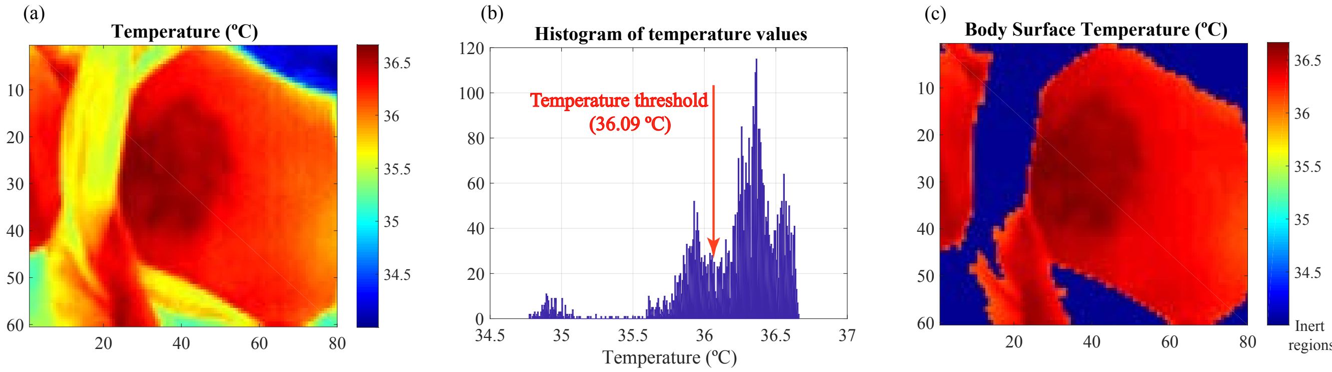

Fig. 11. Example of applying a segmentation algorithm based on Otsu's method to separate the skin from the background and the parts of the body covered by clothes. (a) Original image. (b) Histogram of the image and optimum temperature threshold determined by Otsu's method. (c) Image segmentation after thresholding. The regions in dark blue correspond to the scene background or the patient's clothes.

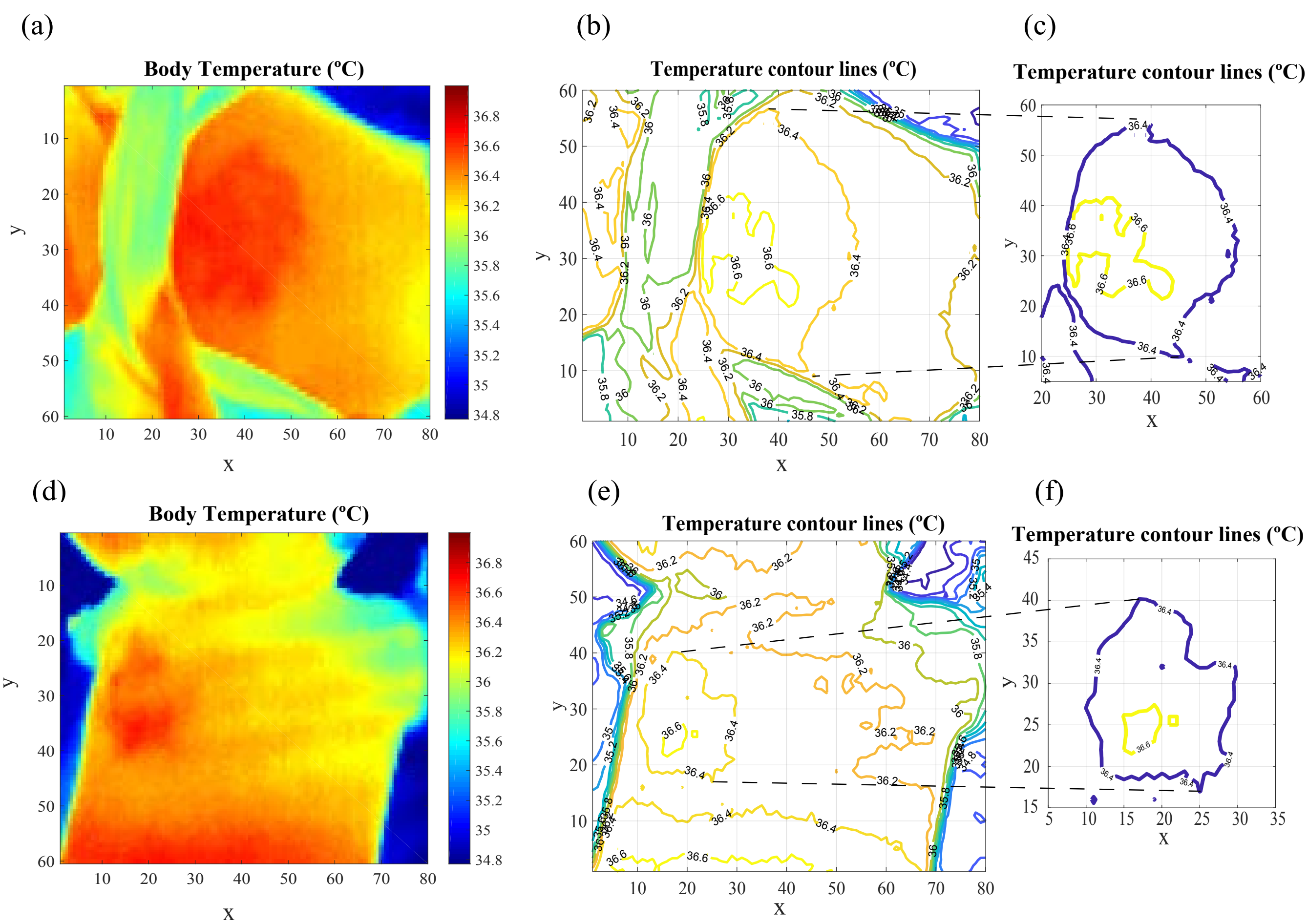

Fig. 12. Evaluation of a hemangioma's size before and after treatment with contour line extraction. Figures (a)-(c) show the original malformation and its area. Figures (d)-(f) show the same malformation after treatment. In both cases, the size of the hemangioma is indicated by temperature contour lines. The area is computed with the coordinate method to compare the patient's response.

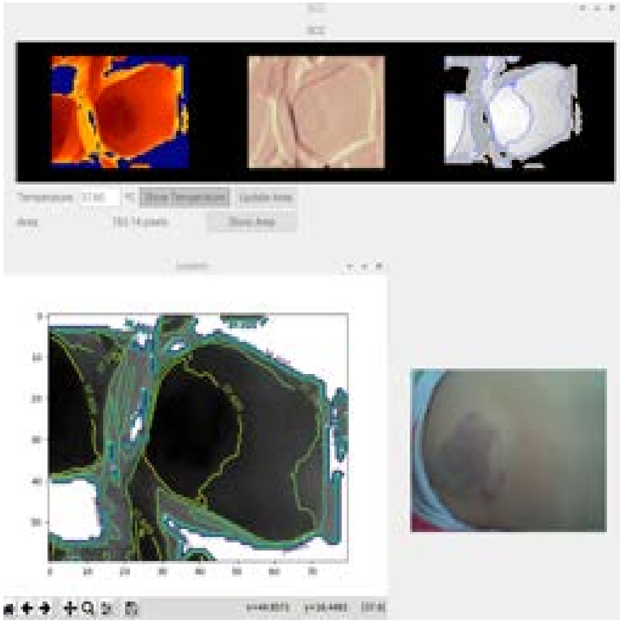

Fig. 13. Custom image processing user interface showing the image processing functions available for infrared images. The original image, represented in the visible spectrum, can be seen at bottom right.

12(a)-(c) correspond to the hemangioma before treatment. Figures 12(d)-(f) are pictures taken after treatment. In the first case, the hemangioma area was 35% smaller after treatment. It should be noted that the method for comparing changes in a hemangioma's area size is invariant to translation and rotation, so the patient does not need to be placed in the same position in each clinical session. The procedure for estimating the size of the region affected by the tumor is described in Listing III.

Listing II: Image segmentation procedure.

1) Histogram counts are computed for the thermal image.
2) Otsu's method is applied using the histogram counts to calculate the optimum temperature threshold value (TH) to segment the image.
3) The image is thresholded: pixel values lower than TH are set to zero.
4) The resulting pixel matrix is stored in the memory.

E. Medical image processing user interface

To facilitate access to the image processing algorithms described above, a custom Graphical User Interface (GUI) was developed in the Python programming language. Python has a powerful programming library to create user interfaces and represent sensor data. The user can obtain a snapshot of an infrared image, calculate its spatial contrast, segment the anomaly, represent its temperature contour lines, and compute the area inside a previously selected contour line.

Use of the GUI is simple and intuitive. The execution time of all the processing algorithms is always below 0.3 ms, so results are immediately available if a particular anomaly needs to be analyzed in detail by the clinician. The GUI is shown in Figure 13. It can be expanded and adapted to a particular research project by adding new or different image processing functions.

(a) (b)

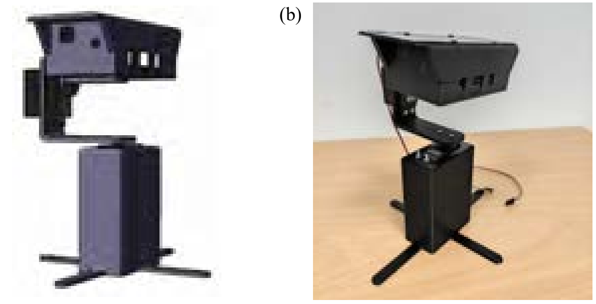

Fig. 14. a) Mechanical design of the system for automatically detecting people with high body temperatures. b) Final system implementation.

Listing III: Contour line extraction procedure.

1) Compute and plot N temperature contour lines within the $[35.5, 38]$ °C range: that is to say, the range in which the temperature usually varies with the presence of vascular anomalies. This was done by selecting the *findContours()* predefined contour extraction routine from the OpenCV library [16].
2) Select a temperature value to delimit the malformation boundary. The same value will be used to compare the area of the affected region in the different clinical sessions. The *findContours()* function provided coordinate pairs $P_i\,(x_i, y_i)$ with $i = 1, \ldots, N$ of the N vertices that delimited the contour line. Note that the vertices have to create a closed contour. The start and end point vertex coordinates are the same and must therefore be taken into account twice in the computation: i.e., $P_1\,(x_1, y_1) = P_N\,(x_N, y_N)$.
3) The corresponding contour line is plotted separately for a detailed analysis.
4) The size (the number of pixels affected by the vascular malformation) is computed using the coordinate method [14], [15], in two steps:

$$S_1 = x_1 y_2 + \sum_{i=1}^{N-1} x_i y_{i+1}, \quad S_2 = x_2 y_1 + \sum_{i=1}^{N-1} x_{i+1} y_i$$
$$Area = \frac{|S_1 - S_2|}{2} \tag{5}$$

V. Case study B: Personal temperature monitoring in public environments

The second application scenario envisaged for the system was the detection of people with fever in public places. For this task, the system casing was redesigned and the touch screen was removed. Figure 14 shows snapshots of the new system casing design and its final implementation. During operation, the acquired images can be optionally streamed, stored, or

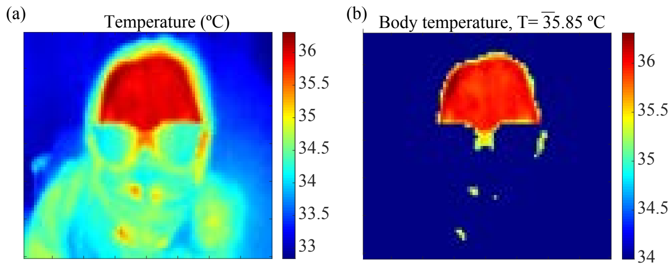

Fig. 15. Illustration of the processing steps for gauging average body temperature. a) Original IR image. b) Segmented IR image. Temperature is estimated by averaging the active pixel values.

displayed on a laptop connected remotely to the sensor. System operation can be automatized or supervised by an operator.

According to the experimental data in Figure 6, to minimize absolute temperature measurement error, the distance between the device and the target has to be bounded. Ideally, the system should be mounted in narrow corridors or checkpoints where the distance to the target is limited and predetermined. In such situations, once the sensor has been calibrated it is possible to estimate absolute measurement error with the experimental data from Figure 6. Two operating modes were devised. Each one is analyzed separately as follows.

A. Temperature monitoring with an operator

In this situation, people pose in front of the camera. An operator triggers a snapshot when a person's face is displayed and their average skin temperature is then determined. The processing steps are detailed in Listing IV.

Listing IV: Measurement of people's average body temperature.

1) A person poses in front of the camera's field of view.
2) An operator triggers a snapshot with the IR camera.
3) IR values are converted to absolute temperature values.
4) Temperature values below and above possible body temperature values are set to zero and not taken into account in the next phases of computation.
5) The skin is segmented using Otsu's thresholding method.
6) Average skin temperature is determined by averaging active pixel temperature values.

The method is illustrated in Figure 15 with a person wearing glasses and a mask. The algorithm segments the skin and averages its temperature to gauge the body temperature. This method is robust to situations in which automatic face detection is challenging due to people wearing glasses, masks, caps, hats, etc.

B. Unsupervised body temperature estimation

In many situations—for example, in crowded public places like stadiums, train stations, etc.—it may be convenient to

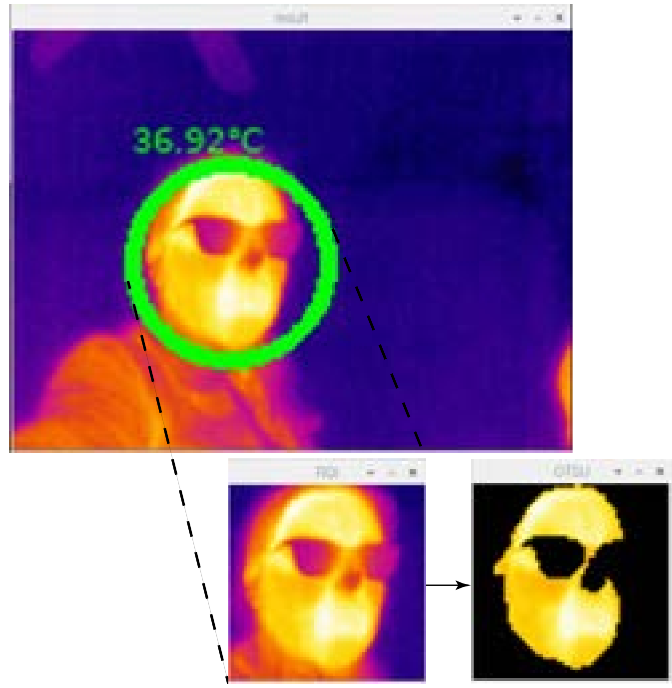

Fig. 16. Automatic face detection and temperature monitoring. a) Infrared image with the ROI and the measured skin temperature. b) ROI detail. c) Result of the ROI skin segmentation with Otsu's method.

automatize body temperature measurement. For this purpose, a face detector was implemented to automatically trigger the body temperature estimation every time a face is detected. We started with a Haar feature-based cascade classifier from the OpenCV library. To train the algorithm, we created an image dataset with infrared images. The dataset contained 750 faces in different poses, including people wearing glasses and masks. This was necessary because some facial features are different in the LWIR band. Noses, for example, usually have lower temperatures than cheeks and may appear as darker regions. Eyes may be invisible because glasses completely filter out the IR radiation.

Figure 16 shows the automatic body temperature detection interface. Every time a face is detected within the visual scene, the algorithm marks it with a colored circle and computes the average face skin temperature, as shown in Figure 16.(a). Figure 16.(b) shows a close-up view of the detected face (Region of Interest, ROI) and Figure 16.(c) shows the result of skin segmentation within the ROI. The pixel intensity values following segmentation are averaged to estimate the body temperature.

The algorithm can be run at a fixed frame rate of up to 35 frames per second. Since the Lepton sensor frame rate is 9 frames per second, in our study this was the maximum achievable execution speed. This frame rate proved to be sufficient to monitor the temperature of non-static people facing the camera lens.

VI. Benchmarking and Future Work

After analyzing existing commercial thermography-based systems, we found several competitive possibilities in the

TABLE III
BENCHMARKING OF DIFFERENT INFRARED SYSTEMS FOR BODY TEMPERATURE MEASUREMENT.

Sensor	Sensitivity ($^{\circ}C$)	Accuracy ($^{\circ}C$)	Precision ($^{\circ}C$)	Range ($^{\circ}C$)	Range (λ)	Resolution	Programa-bility	Hardware expansion
FLUKE TiX560	$\leq$ 0.03	ND (factory calibrated)	$\pm$ 2	$[-20, 1200]$	LWIR & visible	320 $\times$ 240	No	Limited
FLIR A320	$\leq$ 0.05	$\pm$ 0.5 (factory calibrated)	$\pm$ 2	$[-20, 120]$	LWIR	320 $\times$ 240	No	No
Mediterm IRIS 640	0.01	<0.2 (user calibration)	ND	$[17, 38]$	LWIR	640 $\times$ 480	No	No
This system	0.05	<0.1 (user calibration)	$\pm$ 1	$[-10, 80]$	LWIR & visible	160 $\times$ 120	Yes	Yes

market. Some manufacturers, like FLIR [17],], already market general-purpose multispectral vision systems combining infrared and conventional vision sensors, usually with higher pixel resolution and better image quality. However, such imaging systems are not open platforms in which the user can embed specific image processing algorithms. Vendors like Meditherm [6] provide specific infrared cameras for medical applications. These systems are stand-alone infrared cameras which offer no possibility of multispectral vision or image processing in the infrared band. They also need to be connected to a PC, laptop, or tablet via a USB cable to be powered and to display images, and cannot therefore be considered portable systems.

Table III details the features of some representative systems developed by the aforementioned providers. Some of them are factory calibrated and their temperature measurement accuracy is limited by particular operating conditions, i.e., external temperature, distance, size of the target object, optics, etc. In terms of measurement precision, the proposed system is competitive if the target is less than 2 m from the IR sensor.

As an alternative to all the existing commercial solutions with higher image quality, we propose a low-resolution, customizable, low-cost system that is easy to build and adaptable to different research scenarios requiring body temperature analysis. Such adaptation is made feasible at the hardware level by adding extra sensors and peripherals to the system, and at the software level by implementing advanced image processing algorithms. The huge current demand for infrared cameras capable of detecting body temperature in public environments justifies the existence of open-test platforms that can easily be adapted to study the further evolution of the COVID-19 virus. Possible future scenarios associated with the pandemic are still unpredictable and require devices that can easily be customized. Finally, the proposed system is low-cost and based on an open platform. This facilitates its dissemination and sharing among the research community.

VII. CONCLUSIONS

A custom system has been implemented for the acquisition and processing of biomedical infrared images. This article details its full physical implementation and the connectivity between all its components. This is a real-time, autonomous operating system and an open platform suitable for clinical research. We have demonstrated its usefulness in differentiating high- and low-flow vascular malformations. Furthermore, it has been modified to automatically detect people who may be affected by COVID-19. In comparison with other existing alternatives, the system is potentially easier to adapt to different medical scenarios requiring body temperature measurement and image processing.

REFERENCES

[1] A. Saxena and G. Willital, “Infrared thermography: Experience from a decade of pediatric imaging,” *European Journal of Pediatrics*, vol. 167, no. 1, pp. 757–764, August 2008.
[2] J. Hardwicke and O. Titley, “Thermographic assessment of a vascular malformation of the hand: A new imaging modality,” *Journal of Clinical Imaging Science*, vol. 6, no. 1, pp. 6–9, March 2016.
[3] S. Schneider, I. Kohli, I. Hamzavi, M. Council, A. Rossi, and D. Ozog, “Emerging imaging technologies in dermatology: Part I: Basic principles,” *Journal american academy dermatology*, vol. 80, no. 40, pp. 1114–1120, April 2019.
[4] M. García-Romero, A. Chakkittakandiyil, and E. Pope, “The role of infrared thermography in evaluation of proliferative infantile hemangiomas. Results of a pilot,” *International Journal of Dermatology*, vol. 53, no. 3, pp. 216–217, May 2014.
[5] J. Mohammed, A. Balma-Mena, A. Chakkittakandiyil, F. Matea, and E. Pope, “Infrared thermography to assess proliferation and involution of infantile hemangiomas: A prospective cohort study,” *JAMA Dermatology*, vol. 150, no. 9, pp. 964–969, June 2014.
[6] “Meditherm IR cameras manufacturer https://meditherm.com. Last accessed June 2020.”
[7] “Spectrom IR cameras manufacturer https://https://spectronir.com/products/. Last accessed June 2020.”
[8] J. A. Leñnero-Bardallo, C. Serrano, B. Acha, and J. A. P.-C. J. Benabéu-Wittel, “Thermography for the differential diagnosis of vascular malformations,” *Clinical and experimental dermatology*, vol. 1, no. 1, pp. 1–5, August 2020.
[9] S. Behravesh, W. Yakes, N. Gupta, S. Naidu, B. W. Chong, A. Khademhosseini *et al.*, “Venous malformations: clinical diagnosis and treatment,” *Cardiovascular Diagnosis and Therapy*, vol. 6, no. 6, p. 557–569, December 2016.
[10] M. Wassef, F. Blei, D. Adams, A. Alomari, E. Baselga, A. Berenstein *et al.*, “Vascular anomalies classification: Recommendations from the international society for the study of vascular anomalies,” *Pediatrics*, vol. 136, no. 1, p. 203–214, June 2015.
[11] J. Cox, E. Bartlett, and E. Lee, “Vascular malformations: A review,” *Seminars in Plastic Surgery*, vol. 28, no. 2, pp. 58–63, May 2014.
[12] C. Leaute-Labreze, P. Hoeger, J. Mazereeuw-Hautier, L. Guibaud, E. Baselga, G. Posiunas *et al.*, “A randomized controlled trial of oral propranolol in infantile hemangioma,” *New England Journal of Medicine*, vol. 372, no. 1, pp. 735–746, February 2015.
[13] M. Wassef, F. Blei, D. Adams *et al.*, “Vascular anomalies classification: recommendations from the international society for the study of vascular anomalies,” *Pediatrics*, vol. 136, no. 1, pp. 203–2014, July 2015.

[14] R. C. Gonzalez and R. E. Woods, *Digital image processing*. Pearson, 2007.
[15] C. Solomon and T. Breckon, *Fundamentals of Digital image processing*. Wiley-Blackwell, 2010.
[16] "OpenCV repository https://opencv.org/. Last accessed july 2019."
[17] "FLIR LEPTON IR cameras manufacturer https://flir.com. Last accessed June 2020."